Zhao et al. Nanoscale Research Letters (2018) 13:250
https://doi.org/10.1186/s11671-018-2656-5

Nanoscale Research Letters

NANO EXPRESS Open Access

# Effect of Surfactants on the Microstructures of Hierarchical $SnO_2$ Blooming Nanoflowers and their Gas-Sensing Properties

Yan-Fei Zhao[1,2], Yu-Ping Sun[1*], Xiu Yin[1], Guang-Chao Yin[1], Xiao-Mei Wang[1], Fu-Chao Jia[1] and Bo Liu[1*]

## Abstract

Hierarchical $SnO_2$ blooming nanoflowers were successfully fabricated via a simple yet facile hydrothermal method with the help of different surfactants. Here we focus on exploring the promotion effects of surfactants on the self-assembly of 2D $SnO_2$ nanosheets into 3D $SnO_2$ flower-like structures as well as their gas-sensing performances. The polyporous flower-like $SnO_2$ sensor exhibits excellent gas-sensing performances to ethanol and $H_2S$ gas due to high porosity when polyvinyl pyrrolidone is added into the precursor solution as a surfactant. The response/recovery times were about 5 s/8 s for 100 ppm ethanol and 4 s/20 s for 100 ppm $H_2S$, respectively. Especially, the maximum response value of $H_2S$ is estimated to be 368 at 180 °C, which is one or two orders of magnitude higher than that of other test gases in this study. That indicates that the sensor fabricated with the help of polyvinyl pyrrolidone has good selectivity to $H_2S$.

**Keywords:** Tin dioxide, Gas sensor, Surfactant, Nanoflowers

## Background

Gas sensors have attracted a widespread attention due to their potential applications in detecting toxic, noxious, flammable, and explosive gas [1]. At present, the metal oxide semiconductors occupy an important position in various sensors due to their simple preparation process, lower cost, and higher sensitivity to the target gases [2–4]. Tin dioxide ($SnO_2$), a multifunctional n-type material with a direct band gap of 3.6 eV [5], has been widely used in both fundamental study and practical applications, such as gas sensors [6], catalysis [7], and optoelectronic devices [8]. Especially, $SnO_2$ has been regarded as the most potential sensing material owing to its natural non-stoichiometry [9], high sensitivity, fast response/recovery speed, and high chemical stability [10].

It is well known that the gas-sensing mechanism of metal oxides is related to the adsorption and desorption processes of the target gas on the sensor surface, giving rise to a change of the electrical conductivity [11]. These processes strongly depend on the size, morphology, and dimension as well as crystalline structure of the samples [12]. There are two main ways to effectively enhance the sensing performance of $SnO_2$ [13]. One is to synthesize composed materials based on $SnO_2$, such as fabrication of p-n junctions, surface decoration, or doping [14]. The other is to prepare various pure $SnO_2$ materials including nanotubes [15], nanorods [16], nanospheres [17], hollow structures [14], and nanoflowers [18], which have unique nanostructures, high specific surface area, and strong electron capture abilities [19]. Recently, three-dimensional (3D) hierarchical $SnO_2$ nanostructures have drawn much attention because of their better gas-sensing performance caused by large specific surface area and rapid gaseous diffusion compared with 1D and 2D nanostructures [20]. Various techniques have been used to fabricate 3D nanostructures of $SnO_2$ [21], such as chemical vapor deposition [22], solvothermal synthetic method [23], template method [24], sol–gel method [25], and hydrothermal route [26]. Among them, solvothermal and hydrothermal routes with low cost [27], high yields, and simple manipulation have been proved to be the promising methods to synthesize 3D hierarchical $SnO_2$ nanostructures. For instance, Dong et al. prepared hollow $SnO_2$ nanospheres

* Correspondence: sunyuping@sdut.edu.cn; liub@sdut.edu.cn
[1]Laboratory of Functional Molecules and Materials, School of Physics and Optoelectronic Engineering, Shandong University of Technology, Zibo 255000, China
Full list of author information is available at the end of the article

with the diameter ranging from 200 to 400 nm using a solvothermal synthetic method [28]. Li et al. fabricated a novel snowflake-like $SnO_2$ hierarchical architecture with excellent gas-sensing properties via a facile hydrothermal method [29]. Moreover, Chen et al. successfully synthesized hierarchical flower-like $SnO_2$ blooming nanoflowers constructed by self-assembly of many regular-shaped nanosheets through conventional hydrothermal method [30].

The practical application of $SnO_2$ sensors is still limited to a certain extent due to the relative higher working temperature and poorer selectivity to test gases [31]. In order to improve the gas-sensing properties, researchers have paid attention to controllable synthesis of 3D flower-like $SnO_2$ nanostructures with surfactant effects [32], yet a significant challenge is posed because of the variety of surfactants.

In the present study, we report a well-controlled optimization of 3D hierarchical $SnO_2$ nanoflowers based on self-assembly of thin nanosheets with the help of different surfactants under hydrothermal condition. Our systematically comparative gas-sensing study between fabricated sensors focuses on the promotion effect of surfactants on sensor behaviors. The results show that the amphiphilic non-ionic surfactants, such as PVP and Triton X-100, can be potential candidates to optimize the morphology of 3D nanoflowers with high porosity and large specific surface area. Particularly, the sensor based on PVP exhibits high response, fast response time, and good selectivity to $H_2S$ at a relative lower temperature. In addition, a possible well-controlled growth mechanism of $SnO_2$ nanostructures is proposed.

## Methods/Experimental

Trisodium citrate dihydrate and tin chloride dihydrate from Sinopharm Chemical Reagent Co., Ltd. were used as precursors for $SnO_2$ synthesis. Polyethyleneimine, hexamethylene tetramine, TritonX-100, and polyvinylpyrrolidone were purchased from Aldrich Chemistry and used as the structure-directing agents. Distilled water was used throughout the experiments. All chemicals were of analytical grade and used as-purchased without any further purification.

### Synthesis of $SnO_2$ Nanoflowers with Different Architectures

A typical synthesis procedure with simple hydrothermal method can be described as follows (Fig. 1): firstly, 5 mmol of NaOH was added into an 80-ml mixture of anhydrous ethanol and deionized water (1:1) under magnetic stirring. Then, 20 mmol $Na_3C_6H_5O_7{\cdot}2H_2O$ and 10 mmol $SnCl_2{\cdot}2H_2O$ were dissolved into the mixed solution successively under vigorous stirring for 1 h at room temperature. The mixed solution was then transferred into a 100-mL Teflon-lined stainless steel autoclave, and maintained at 180 °C for 12 h, and then cooled down to room temperature naturally. After reaction, the obtained precipitate was collected by centrifugation, washing with deionized water and anhydrous ethanol for several times, and dried at 60 °C for 6 h. The $SnO_2$ nanoflowers were finally obtained after calcining the precipitate in a muffle furnace under air ambient condition at 500 °C for 2 h. In order to synthesize $SnO_2$ nanoflowers with different microstructures, different surface active agents (1.0 g) were introduced into the solution respectively before the dissolution of $Na_3C_6H_5O_7{\cdot}2H_2O$. In this work, four different kinds of surfactants were used, including PVP, PEI, HMT, and TritonX-100, and the corresponding final products are named as $S_{PVP}$, $S_{PEI}$, $S_{HMT}$, and $S_{TritonX\text{-}100}$, respectively, while the product without surfactant is signed as $S_0$.

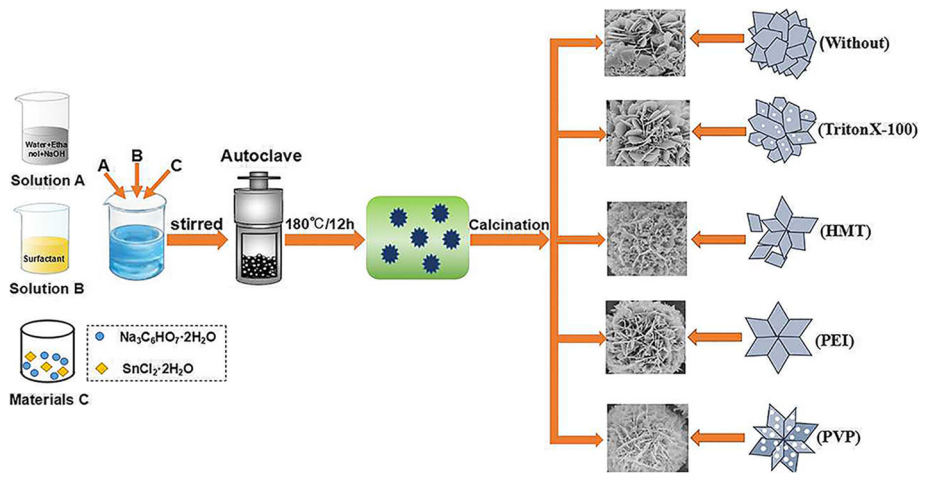


**Fig. 1** Schematic illustration of the formation process of the hierarchical flower-like $SnO_2$ nanostructures using different kinds of surfactants

### Characterizations

It is well known that the gas-sensing properties of gas sensors are highly related to the morphology, size, and dispersibility of nanomaterials. The as-prepared products were analyzed in terms of their structures and morphologies by means of polycrystalline X-ray diffraction (XRD, Germany Bruker AXS D8 Advance), scanning electron microscopy (SEM, USA FEI Sirion 200), and field emission transmission electron microscopy (FETEM, USA Tecnai G2 F20 S-TWIN). The surface area is measured using Elemental Analyzer (USA ASAP 2460) based on the Brunauer-Emmett-Teller (BET) method.

### Sensor Fabrication and Gas-Sensing Test

The gas sensor was fabricated using screen printing method on top of an alumina tube (seen in Fig. 2a). Typically, a proper amount of as-prepared powder was firstly mixed with anhydrous ethanol to form a slurry suspension. Subsequently, the slurry suspension was coated onto the alumina tube by a small brush, which is supported by two Au electrodes and four Pt conducting wires. Next, a Ni-Cr heating wire was inserted into the alumina tube to control working temperature by tuning the heating voltage. Finally, the product was aged at 80 °C for 72 h before testing.

The gas-sensing properties were measured using chemical gas sensor-4 temperature pressure small (CGS-4TPs) intelligent gas-sensing analysis system (Beijing Elliott Technology Co., Ltd., China) under the lab conditions. Figure 2b displays the typical schematic electrical circuit. $R_s$ is the resistance of sensor and $R_l$ is the load resistance, and a heating voltage ($V_h$) is used to adjust the working temperature. In the present work, the response of the sensor was defined as $S = (R_s - R_g)/R_g$, where Rs is the initial resistance and Rg is the resistance after injection of gases. The response and recovery times are defined as the time taken by the sensor to achieve 90% of the total resistance change in the case of adsorption and desorption, respectively.

## Results and Discussion

### Structural and Morphological Characterization

The crystalline phase of the as-prepared $SnO_2$ products was identified by power X-ray diffraction as shown in Fig. 3. From the XRD pattern, all the observed diffraction peaks can be easily assigned to the tetragonal rutile structure of pure $SnO_2$ with the standard JCPDS file card no. 41-1445, and no other peaks can be identified due to impurities. The sharp peaks indicate the high degree of crystallinity of our $SnO_2$ samples, and no remarkable shift is detected in the diffraction peaks, revealing that the samples are of high purity.

Figure 4a shows the SEM image of the product without surfactant. A hierarchical flower-like architecture can be observed and the unique nanoflowers are assembled by ultrathin nanosheets with an average thickness of 20 nm around. Unfortunately, these nanosheets are closely staggered with respect to each other, which results in a sharp decrease in its reaction spaces. Figure 4b–e shows the morphologies of the products obtained by introducing different surface active agents while keeping other experimental conditions unchanged. One can see that upon addition of TritonX-100 surfactant (Fig. 4b), the nanosheets are loosely intersected with each other, and some mesopores are shaped at the edge of the nanosheets. When HMT was added into the reaction mixture as the surface active agents (Fig. 4c), it can be seen that the nanosheets are arranged randomly and a number of smaller nanosheets are formed between ultrathin nanosheets. Figure 4d shows the SEM images of the products obtained by introducing PEI surfactant in the precursor solution, which reveals that the nanosheets with smooth surfaces are arranged orderly and are vertically intersected with each other, leaving a larger reaction space. Figure 4e, f presents the typical SEM images of the products obtained upon addition of PVP surfactant under the same conditions. One can see that the nanosheets are uniformly distributed along the radius across the whole sample to form a flower-like structure. Moreover, compared with other structures of $S_{TritonX\text{-}100}$, $S_{HMT}$, and $S_{PEI}$, the nanosheets of $S_{PVP}$ are enclosed into an inverted triangle cone with a relative larger hollow space (Fig. 4e). Further enlarged image reveals that the flower-like architectures are assembled by mesoporous nanosheets to form an open porous hierarchical

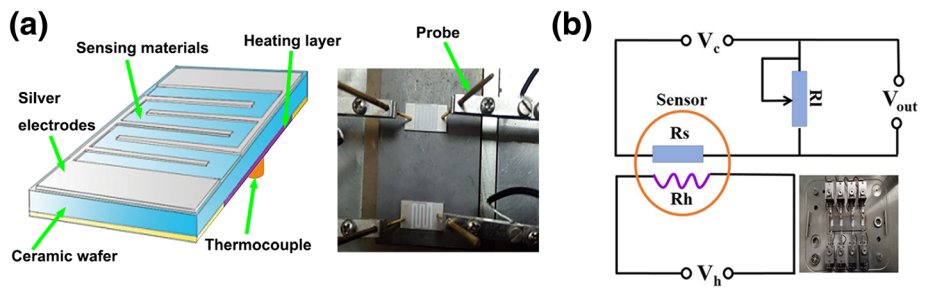


**Fig. 2** **a** Schematic diagram of the gas sensor configuration. **b** Electric circuit diagram of sensor device

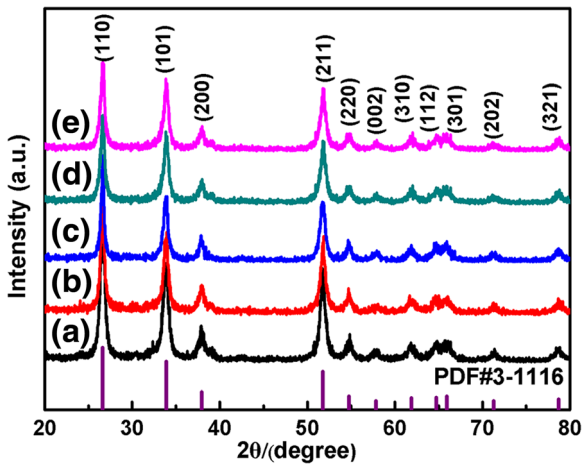


**Fig. 3** XRD patterns of the $SnO_2$ samples with different morphologies. **a** $S_0$, **b** $S_{TritonX100}$, **c** $S_{HMT}$, **d** $S_{PEI}$, and **e** $S_{PVP}$

structure, and each nanosheet was fabricated with numerous mesopores (Fig. 4f).

In order to further investigate the microstructures and crystalline properties of the nanoflowers, low-magnification TEM and typical HRTEM combined with the selected area electron diffraction (SAED) analysis techniques are employed. From TEM images (Fig. 5a–e), it can be seen that the nanoflowers with an average diameter of 3 μm are assembled of numerous individual nanosheets, and its morphology and size are similar to the SEM images. Especially, the TEM image of $S_{PVP}$ (Fig. 5e) shows that the most flower-like structure with the uniform dark color in the middle region is constructed from the well dispersion of numerous uniform nanosheets along the radius direction. Combining the SEM with TEM measurements, a conclusion can be drawn that the structures obtained upon the addition of PVP surfactant are the most stable. The high-resolution TEM (HRTEM) images show that for samples $S_0$, $S_{HMT}$, $S_{PEI}$, and $S_{PVP}$, the observed 0.335-nm lattice spacing is consistent with the (110) lattice plane of tetragonal rutile $SnO_2$ (Fig. 5f only shows a typical HRTEM image for $S_{HMT}$ as a representative). The exposure of (110) lattice plane reveals that (110) lattice plane is the most stable plane for $SnO_2$ in air, which is consistent with the theoretical study. It should be noted that $S_{TritonX\text{-}100}$ is a special case in this work (Fig. 5b). Upon addition of TritonX-100 surfactant, the growing and the dispersion of nanosheets are randomly leading to a relative larger diameter (3~4 μm ) of the nanoflowers compared with other samples. Moreover, its HRTEM image shows that the calculated lattice spacing is 0.264 nm, which is corresponding to (101) lattice plane of tetragonal rutile structure of $SnO_2$. Furthermore, SAED pattern reveals

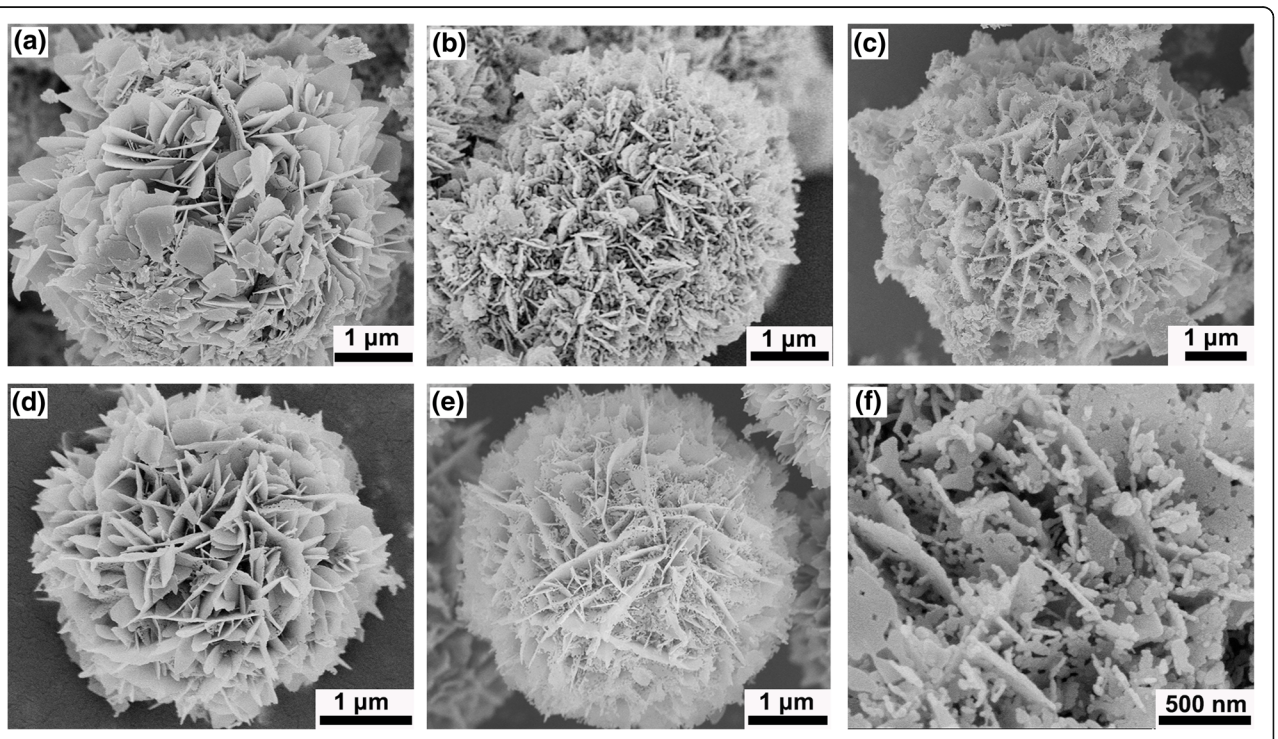


**Fig. 4** The SEM images of the $SnO_2$ nanoflowers with different morphologies. **a** $S_0$, **b** $S_{TritonX\text{-}100}$, **c** $S_{HMT}$, **d** $S_{PEI}$, and **e**, **f** $S_{PVP}$

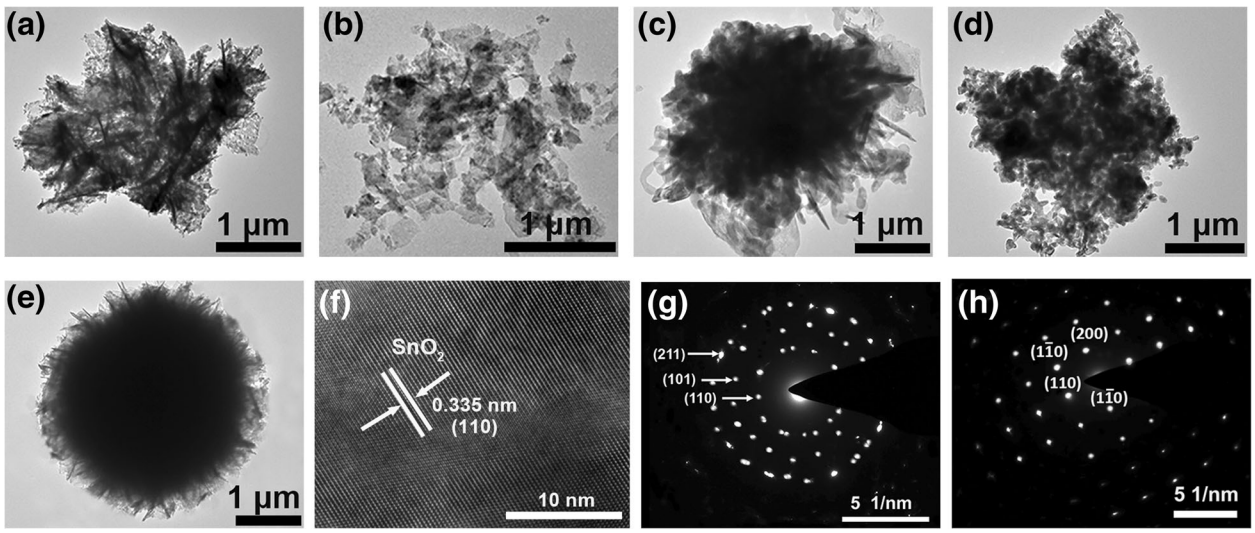


**Fig. 5** Low-magnification TEM images of $SnO_2$ samples. **a** $S_0$, **b** $S_{TritonX\text{-}100}$, **c** $S_{HMT}$, **d** $S_{PEI}$, and **e** $S_{PVP}$. **f** HRTEM micrograph showing enlarged lattice images of $S_{HMT}$. **g** SAED patterns of $S_0$. **h** SAED patterns of $S_{PVP}$

that $S_{PVP}$ has a nearly perfect single crystalline structure, and the diffraction spots correspond to (110),($1\bar{1}0$), ($\bar{1}10$), and (200) lattice planes of $SnO_2$ (Fig. 5h). Contrarily, for other samples such as $S_0$, $S_{HMT}$, $S_{PEI}$, and $S_{TritonX\text{-}100}$, the SAED pattern shows a polycrystalline structure, and the diffraction ring is indexed to the (110), (101), and (211) planes of tetragonal rutile structure of $SnO_2$ (Fig. 5g).

### Growth Mechanism of the $SnO_2$ Nanoflowers

Based on the experimental observations and analysis above, it is believed that the surfactants play a significant role in the formation of various $SnO_2$ nanoflowers [33]. The possible growth mechanism of hierarchical sheet-flower $SnO_2$ nanostructures is briefly illustrated in Fig. 1. In this work, all $SnO_2$ nanoflowers are synthesized using $SnCl_2$ as precursor [34]. Under the hydrothermal conditions, the overall reaction for the growth of $SnO_2$ crystals with high temperature and pressure can be expressed as follows [35]:

$$SnCl_2 + 2OH^- \rightarrow Sn(OH)_2 + 2Cl^- \quad (1)$$

$$Sn(OH)_2 \rightarrow SnO + H_2O \quad (2)$$

$$SnO + \frac{1}{2}O_2 \rightarrow SnO_2 \quad (3)$$

$$Sn(OH)_2 + \frac{1}{2}O_2 + H_2O \rightarrow Sn(OH)_4 \rightarrow SnO_2 + 2H_2O \quad (4)$$

During the whole process, three chemicals greatly affect the morphology growth of $SnO_2$ nanoflowers, including NaOH, sodium citrate, and the surfactant. Firstly, a number of tiny primary nanocrystals were formed due to the hydrolysis of $Sn^{2+}$ in a basic ethanol-water solution as well as its rapid reaction with $OH^-$ ions from NaOH. It should be noted that the basic ethanol-water environment is significant for stimulating the $SnO_2$ nucleation and growth [36]. The addition of sodium citrate plays a crucial role in the space distribution of precursors due to its strong coordinating ability, which can promote an anisotropy in the fast growth and aggregation of $SnO_2$ nanosheets with the driving force of decreasing surface energy and accelerate the assembling of nanosheets into the stable hierarchical blooming nanoflowers [37].

Generally, the addition of surfactants is favorable for the enlargement of the surface area as well as the enhancement of the surface activity [38]. Among the surfactants used in this work, PEI is one kind of cationic surfactants. When PEI is added into the reaction solutions, due to the existent $N^+$ ions with a hydrophilic tail, PEI will preferentially adsorb on a certain crystal facet, which is conducive to the nucleation of $SnO_2$ nanocrystals as well as the orderly growth of $SnO_2$ nanosheets with a directional selectivity. Both PVP and TritonX-100 are amphiphilic non-ionic surfactants, which can serve as a soft template in the fabrication of mesoporous materials. Let us take PVP for example to explain the growth mechanism of porous structures on the $SnO_2$ nanosheets as follows: when PVP is added into the solution, PVP molecules self-assemble into spherical micelles because of the strong hydrophobic attraction between the straight alkyl tails. Due to its amphiphilicity, the hydrophilic radical will move toward the direction of aqueous solution, and the hydrophobic radical will move in the opposite direction, leading to the formation of

inorganic domains around periodically arranged PVP micelles. Then, $Sn^{2+}$ and $OH^-$ ions are easily adsorbed on the outer surfaces of these micelles via electrostatic interactions until $SnCl_2$ is oxidized into $SnO_2$ nanosheet, which are followed by the self-assembly of nanosheets into blooming nanoflowers with the help of sodium citrate. Finally, the soft-template PVP micelles are removed during the calcination process, yielding hierarchical $SnO_2$ nanoflowers with mesoporous structures. Although both PVP and Triton X-100 contributed to the formation of porous structures, it should be noted that PVP can also play a role of dispersing agent, which makes the $SnO_2$ nanosheets grow more uniformly and separately owing to the strong interactions and short electrostatic interaction distances between the $SnO_2$ nanosheets and PVP.

## Gas-Sensing Properties

As reported previously, the hierarchical flower-like nanostructures were favorable for the absorption and diffusion of probe gases in sensor materials. To shed light on the promotion effect of surfactants and corresponding morphology on sensor behavior, a systematically comparative gas-sensing study between fabricated sensors is performed in this work.

### *Gas-Sensing Behaviors of Fabricated Sensors to Ethanol*

The optimum operating temperature is a key factor for the application of semiconductor oxide gas sensors. Firstly, the responses of sensors to 100 ppm ethanol gas at various operating temperatures from 180 to 360 °C are tested as shown in Fig. 6a. It is clearly observed that all these sensors exhibit a similar gas-sensing behavior, i.e., the response values first increase with a rise of temperature, reach a maximum value at 270 °C, and then decrease gradually with a further increasing of temperature. Therefore, 270 °C can be chosen as the optimized operating temperature for gas-sensing study of all fabricated flower-like $SnO_2$ sensors in our work. The reason for the dependence of the response on the temperature is as follows: When the operating temperature is too low, a relative smaller response value is assigned to the inert response due to chemical activation, while for too high operating temperature, the absorbed gas target molecules can escape from the sensors before reactions, resulting in a poor response as well. In addition, it can be seen from Fig. 6a that of all the five $SnO_2$ sensors based on different surfactants, $S_{PVP}$ shows the highest response to ethanol gas and the largest gas response value (38). The maximum response values of other four sensors are 27 for $S_{PEI}$, 16 for $S_{HMT}$, 11 for $S_{TritonX\text{-}100}$, and 8 for $S_0$.

Figure 6b shows the response of all $SnO_2$ sensors toward ethanol in the concentration range 10~150 ppm at the optimal work temperature 270 °C. It can be clearly observed that the response of all sensors increases rapidly with the gas concentration below 50 ppm, and this trend becomes smooth from 50 to 150 ppm, tending to be saturated at about 100 ppm. As expected, the surfactants and the induced morphologies can produce a large

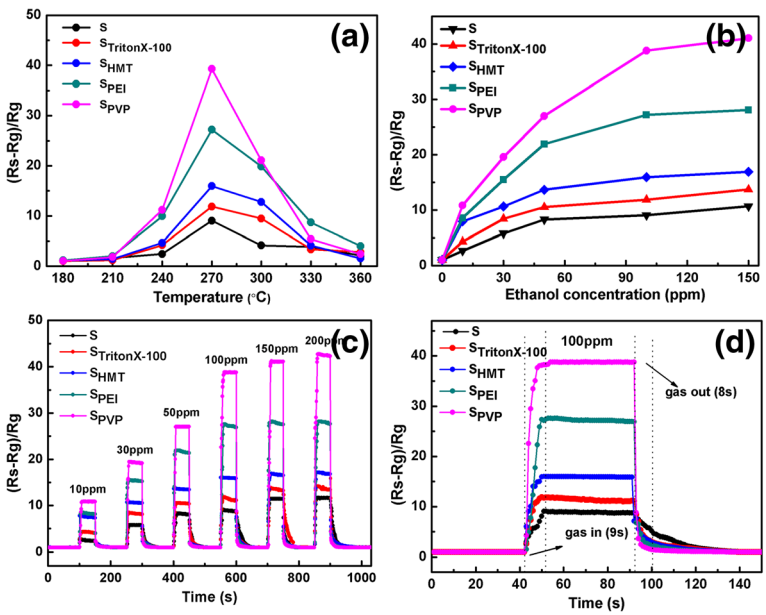


**Fig. 6** **a** The response of the sensors to 100 ppm ethanol under different operating temperatures (180–360 °C). **b** The dynamic response curves of the sensors to ethanol with different concentrations (10–150 ppm) at 270 °C. **c** Response versus time curves of the sensors to 10–200 ppm ethanol consecutively at 270 °C. **d** Dynamic sensing transient of the sensors to 100 ppm ethanol at 270 °C

influence on the gas-sensing of fabricated sensors. Among these fabricated sensors, the $S_{PVP}$ sensor exhibits the best sensing behavior toward ethanol gas, and $S_{PEI}$ comes second. To get a deep insight of gas-sensing mechanism, BET (Brunaure-Emmett-Teller) nitrogen adsorption-desorption is also performed to determine the specific surface areas of these samples, as shown in Table 1. One can see that $S_{PEI}$ has the largest specific surface area (38.4 $m^2 g^{-1}$) with overall majority. It is noteworthy that despite the relative smaller surface area (15.5 $m^2 g^{-1}$), $S_{PVP}$ is the best candidate for ethanol gas sensor due to its perfect flower-like architecture with orderly stacking self-assembly and relative higher porosity, providing more active adsorption sites for ethanol molecules. Even at low ethanol concentration as 10 ppm, the sensitivity of $S_0$, $S_{TritonX\text{-}100}$, $S_{HMT}$, $S_{PEI}$, and $S_{PVP}$ sensors can reach 2, 4, 7, 9, and 11, respectively, indicating their potential application for ethanol sensors even at low concentrations.

Figure 6c displays dynamic gas-sensing response and recovery curves of fabricated sensors toward ethanol with an operating temperature of 270 °C, from which one can see that the responses of all fabricated sensors increase with increasing the ethanol concentration, and a remarkable modulation of resistance is achieved at about 100 ppm. The responses show a drastic rise once the sensor was exposed to target gases and then dropped to its initial value in air. As shown in Fig. 6d, the response and recovery time to 100 ppm ethanol are about 16 s and 28 s for $S_0$, 14 s and 18 s for $S_{TritonX\text{-}100}$, 11 s and 15 s for $S_{HMT}$, 9 s and 11 s for $S_{PEI}$, and 5 s and 8 s for $S_{PVP}$, respectively. It is obvious that the $S_{PVP}$ sensor has the best response/recovery characteristics compared with other sensors.

Table 2 shows a comparison of ethanol-sensing performances based on different $SnO_2$ fabricated approaches reported in other literatures and this work at the concentration of 100 ppm. One can see that our polyporous $SnO_2$ nanoflower presents remarkably ethanol-sensing behaviors with lower optimal operating temperature and higher response value as well as faster response-recovery time, which could be attributed to the presence of numerous mesopores in SPVP sensor, leading to a high porosity in favor of the adsorption and diffusion of ethanol gas.

### *Gas-Sensing Behaviors of Fabricated Sensors to $H_2S$*

As discussed in the previous subsection, $S_{PVP}$ sensor exhibits the best gas-sensing property to 100 ppm ethanol owing to its high porosity. In order to find out its optimum detecting gas, we test the response of $S_{PVP}$ sensor toward different gases, including acetone, methanol, formaldehyde, and $H_2S$, with a concentration of 100 ppm at various operating temperatures (as shown in Fig. 7a, b). It can be noted that the optimal response appears at 330 °C of methanol, at 210 °C of formaldehyde, at 360 °C of acetone, and at 180 °C of $H_2S$. Furthermore, the maximum response value of $S_{PVP}$ to $H_2S$ is estimated to be 368, which is one or two orders of magnitude ($S_{H_2S}/S_{ethanol} = 9$, $S_{H_2S}/S_{formaldehyde} = 45$) higher than that to other test gases. The lowest optimal work temperature as well as the best response value indicates $S_{PVP}$ has the excellent selectivity to $H_2S$.

Considering the high response of $S_{PVP}$ sensor to $H_2S$, we also performed a systematic gas-sensing measurement of all other sensors. A dynamic gas-sensing response and recovery curves of fabricated sensors toward $H_2S$ at 180 °C are displayed in Fig. 7c. Obviously, the response values of all fabricated sensors show a monotonic increasing function of $H_2S$ concentration. For 100 ppm $H_2S$, the response and recovery time are about 9 s and 43 s for $S_0$, 5 s and 30 s for $S_{TritonX\text{-}100}$, 14 s and 40 s for $S_{HMT}$, 8 s and 38 s for $S_{PEI}$, and 4 s and 20 s for $S_{PVP}$, while the maximum response values are 35, 132, 41, 49, and 368 for $S_0$, $S_{TritonX\text{-}100}$, $S_{HMT}$, $S_{PEI}$, and $S_{PVP}$, respectively. It is obvious that the $S_{PVP}$ sensor has the best response/recovery characteristics and the highest response to $H_2S$ gas compared with other sensors, while $S_{TritonX\text{-}100}$ achieves the second.

**Table 2** The comparison of ethanol sensing performances of $SnO_2$ materials based on different fabricated approaches reported in other literatures and this work

| Materials | Synthetic methods | Working temperature (°C) | Sensor response | Response/recovery time (s) | Reference |
|---|---|---|---|---|---|
| $SnO_2$ nanoparticles | Hydrothermal route | 300 | 19.4 | 4.4/23.2 | [1] |
| $SnO_2$ hollow microspheres | One-step calcined method | 320 | 31.2 | 5.2/8.3 | [2] |
| $SnO_2$ nanoflowers | Hydrothermal method | 240 | 6.9 | 25/60 | [3] |
| $SnO_2$ microstructure | Hydrothermal method | 300 | 10 | 6/52 | [4] |
| $SnO_2$ nanorods | Hydrothermal route | 300 | 13.8 | 5/60 | [5] |
| $SnO_2$ nanoflowers | Hydrothermal method | 270 | 38.7 | 5/8 | This work |

**Table 1** The BET for the prepared samples

| Morphology | $S_0$ | $S_{TritonX\text{-}100}$ | $S_{HMT}$ | $S_{PEI}$ | $S_{PVP}$ |
|---|---|---|---|---|---|
| BET | 14.5 $m^2 g^{-1}$ | 14.6 $m^2 g^{-1}$ | 15.2 $m^2 g^{-1}$ | 38.4 $m^2 g^{-1}$ | 15.5 $m^2 g^{-1}$ |

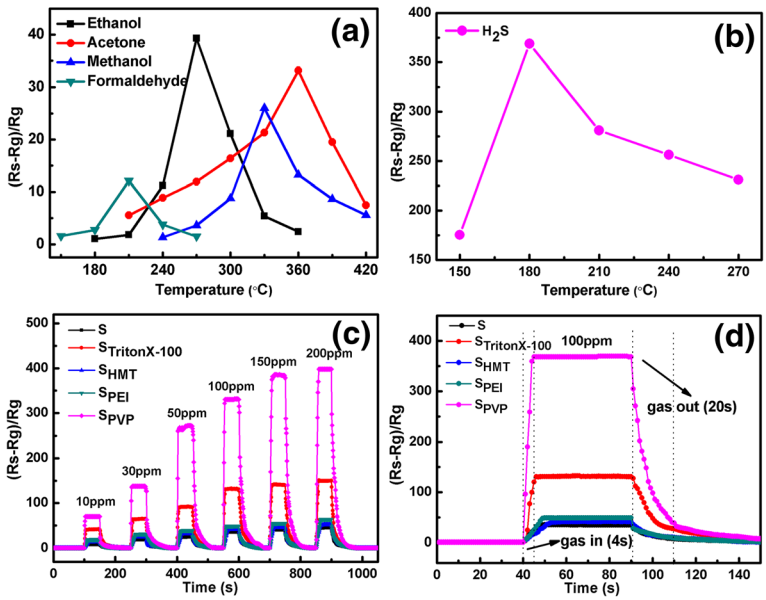


**Fig. 7** **a** Response of $S_{PVP}$ sensor to 100 ppm ethanol, acetone, methanol, and formaldehyde at different operating temperatures. **b** Response of $S_{PVP}$ sensor to 100 ppm $H_2S$ at different operating temperatures. **c** Response versus time curves of the sensors to 10–200 ppm $H_2S$ consecutively at180 °C. **d** Dynamic sensing transient of the sensors to 100 ppm $H_2S$ at 180 °C

Figure 8 displays the bar graph of response of five fabricated sensors to formaldehyde, methanol, ethanol, acetone, and $H_2S$. All of the gases were tested with a concentration of 100 ppm at the optimal operating temperature. $S_{TritonX\text{-}100}$ and $S_{PVP}$ show a distinct response to $H_2S$, while $S_{PEI}$ shows the highest gas response to methanol and acetone. It should be mentioned that the specific surface area and the porosity are two important factors for gas sensors. The larger specific surface area will provide more active sites for adsorption and desorption of test gases, while the larger porosity would induce a greater speed of gas diffusion owing to the presence of mesopores. In comparison, $S_{PEI}$ possesses a relative larger specific surface area than others (seen in Table 1), which shows the highest gas response to methanol and acetone (Fig. 8), while $S_{PVP}$ and $S_{TritonX\text{-}100}$ exhibit the higher gas response to $H_2S$ due to their polyporous flower-like nanostructures, proving good selectivity of $S_{TritonX\text{-}100}$ and $S_{PVP}$ toward $H_2S$. The good selectivity of the samples to $H_2S$ can be explained as follows: when the $SnO_2$ sensor is exposed in $H_2S$ gas, both chemisorbed oxygen species and $SnO_2$ nanostructure react with $H_2S$ during sensing measurement to form $SO_2$ and $SnS_2$, respectively. Compared with $SnO_2$, the body resistance of $SnS_2$ is relatively smaller, leading to the sensitivity enhancement of the gas sensor [39]. On the contrary, the $SnO_2$ sensor does not react with any other target gases, such as formaldehyde, methanol, ethanol, and acetone.

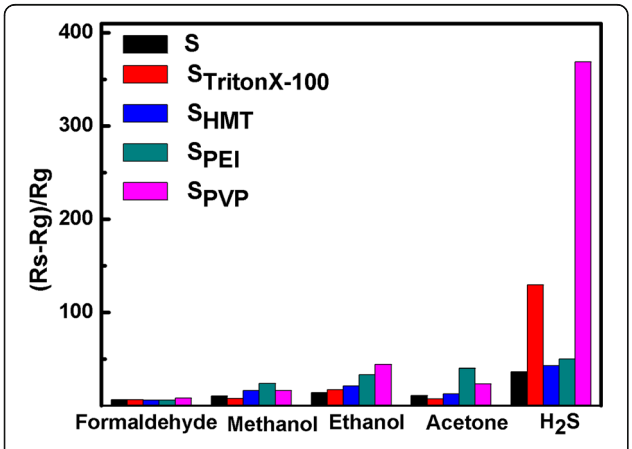


**Fig. 8** The comparison among sensor response of $SnO_2$ nanomaterials to 100 ppm of various gases at the optimal operating temperature

Good stability and long service duration are expected from the viewpoint of practical application. To verify the stability of the sensor, the successive gas-sensing behavior of $S_{PVP}$ to 100 ppm ethanol was tested under the same conditions after 1 month. The samples were stored in the vacuum drying vessel during the 1-month interval. It can be seen from Fig. 9 that $S_{PVP}$ exhibits an excellent repeatability and stability even after 1 month. The three cyclic curves are similar to that measured 1 month ago, including the response value as well as the response-recovery time.

## Gas-Sensing Mechanism

Up to now, the most widely accepted gas-sensing mechanism of semiconductor oxide is the model based on the

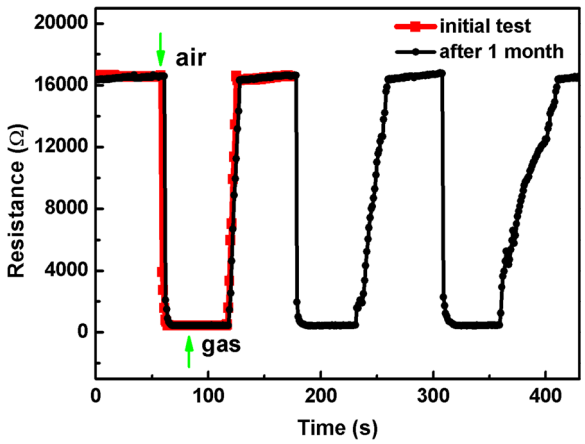


**Fig. 9** Stability of $S_{PVP}$ over 1 month of aging for 100 ppm ethanol at 270 °C

electron transfer dynamics during an adsorption–oxidation–desorption process, which can change the resistance value of the sensors [40]. The response of typical n-type semiconductor greatly depends on the electron concentration. As shown in Fig. 10, at elevated temperature, electrons in the valence band are thermally excited to the conductive band. Once the $SnO_2$ sensor is exposed to ambient air, oxygen molecules will be chemisorbed on the surface of $SnO_2$ nanoflowers. Oxygen ions ($O_2^-$, $O^-$, and $O^{2-}$) are then formed by capturing electrons from the conductive band of $SnO_2$ [41], which is accompanied by an effective enlargement of electron-depleted layer. As a typical n-type semiconductor, the broadening of electron-depleted region means the decrease of carrier concentration within $SnO_2$ nanoflowers, which will lead to the increase of resistance of the sensors. Conversely, when the $SnO_2$ sensor is exposed in the reductive ambient, the absorbed oxygen species will quickly react with the target gas, which results in releasing the trapped electrons back to the conduction band and a reduction of the resistance of the sensors. Among the sensors fabricated in this work, $S_{PEI}$ and $S_{PVP}$ show relative better gas-sensing performances. The underlying physical mechanisms are as follows: the gas sensing properties are strongly dependent on the surface special area and the porosity. In comparison, $S_{PEI}$ possesses a relative larger specific surface area than others, which will provide more active sites for adsorption and desorption of test gases. $S_{PVP}$ exhibits a relative higher porosity due to the polyporous flower-like nanostructures, which is favorable to the rapid diffusion of gas (as shown in Fig. 10).

## Conclusions

We have successfully prepared the 3D hierarchical flower-like $SnO_2$ nanostructures through a simple and low-cost facile hydrothermal route with the assistance of different surfactants. The images of SEM and TEM showed that the fabricated 3D hierarchical $SnO_2$ nanoflowers with an average diameter of 2~4 μm were composed of many 2D nanosheets. The addition of surfactant plays an important role in the formation of nanoflowers. Based on the experimental observations, the possible growth process and gas-sensing mechanism

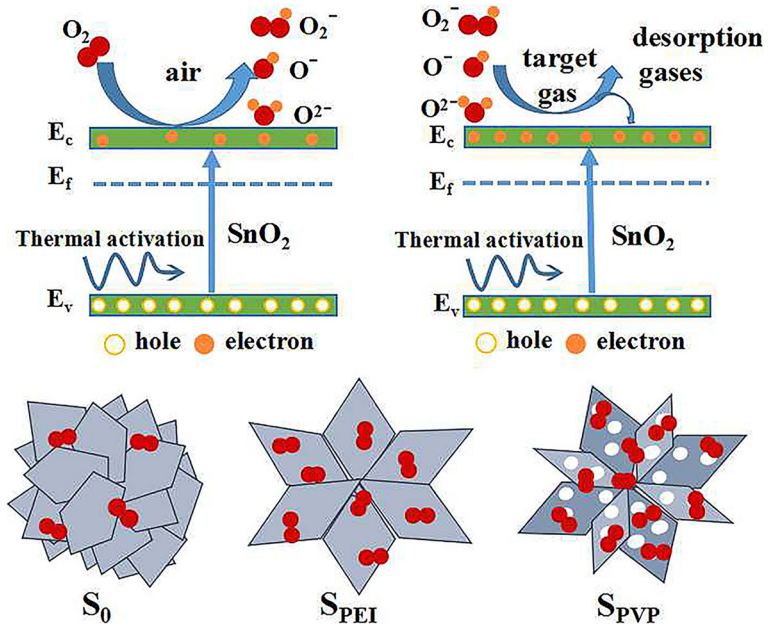


**Fig. 10** Schematic diagrams on the gas-sensing mechanism of flower-like $SnO_2$ hierarchical nanostructures

of $SnO_2$ nanoflowers were proposed. As a cationic surfactant, the addition of PEI is conducive to the nucleation of $SnO_2$ nanocrystals as well as the orderly growth of $SnO_2$ nanosheets, leading to a relative larger specific surface area. As amphiphilic non-ionic surfactants, PVP and TritonX-100 can make the nanosheets grow more uniformly and separately, which can serve as a soft template in the synthesis of advanced material, especially in the fabrication of mesoporous materials. In comparison, the sensor with the help of PVP ($S_{PVP}$) exhibits excellent gas-sensing performances to ethanol and $H_2S$ due to its relative higher porosity. Especially, $S_{PVP}$ shows a high response (368), fast response/recovery time (4 s/20 s), and good selectivity toward $H_2S$ gas. In addition, it is found that NaOH and sodium citrate are also important for the morphological formation of $SnO_2$ nanoflowers.

#### Abbreviations

1D: One-dimensional; 2D: Two-dimensional; 3D: Three-dimensional; BET: Brunauer-Emmett-Teller; FETEM: Field emission transmission electron microscopy; HMT: Hexamethylene tetramine; $Na_3C_6H_5O_7{\cdot}2H_2O$: Trisodium citrate dihydrate; PEI: Polyethyleneimine; PVP: Polyvinylpyrrolidone; SAED: Selected area electron diffraction; SEM: Scanning electron microscopy; XRD: X-ray diffraction

#### Funding

This work was funded by the National Natural Science Foundation of China (no. 11204163 and no. 61704098), Doctoral Foundation of Shandong Province (no. BS2013SF018), and Natural Science Foundation of Shangdong Province (no. ZR2017BF025).

#### Availability of Data and Materials

The datasets supporting the conclusions of this article are included within the article.

#### Authors' Contributions

YS guided the experiments and test process and revised the paper. YZ synthesized the products, analyzed the data, and prepared the manuscript. All authors discussed the results and commented on the manuscript. All authors read and approved the final manuscript.

#### Ethics Approval and Consent to Participate

Not applicable.

#### Consent for Publication

Not applicable.

#### Competing Interests

The authors declare that they have no competing interests.

## Publisher's Note



#### Author details

[1]Laboratory of Functional Molecules and Materials, School of Physics and Optoelectronic Engineering, Shandong University of Technology, Zibo 255000, China. [2]School of Materials Science and Engineering, Shandong University of Technology, Zibo 255000, China.

Received: 14 June 2018 Accepted: 6 August 2018
Published online: 22 August 2018

#### References

1. Li T, Wu Y, Huang J, Zhang S (2017) Gas sensors based on membrane diffusion for environmental monitoring. Sensors Actuators B Chem 243: 566–578
2. Abideen ZU, Kim J-H, Kim SS (2017) Optimization of metal nanoparticle amount on $SnO_2$ nanowires to achieve superior gas sensing properties. Sensors Actuators B Chem 238:374–380
3. Bai S, Wu W, Qin Y, Cui N, Bayerl DJ, Wang X (2011) High-performance integrated ZnO nanowire UV sensors on rigid and flexible substrates. Adv Funct Mater 21(23):4464–4469
4. Liu J, Wu W, Bai S, Qin Y (2011) Synthesis of high crystallinity ZnO nanowire array on polymer substrate and flexible fiber-based sensor. ACS Appl Mater Interfaces 3(11):4197–4200
5. Kamble DL, Harale NS, Patil VL, Patil PS, Kadam LD (2017) Characterization and $NO_2$ gas sensing properties of spray pyrolyzed $SnO_2$ thin films. J Anal Appl Pyrolysis 127:38–46
6. Hijazi M, Rieu M, Stambouli V, Tournier G, Viricelle J-P, Pijolat C (2018) Ambient temperature selective ammonia gas sensor based on $SnO_2$-APTES modifications. Sensors Actuators B Chem 256:440–447
7. Luo W, Fu Q, Zhou D, Deng J, Liu H, Yan G (2013) A surface acoustic wave $H_2S$ gas sensor employing nanocrystalline $SnO_2$ thin film. Sensors Actuators B Chem 176:746–752
8. Woo H-S, Hwang I-S, Na CW, Kim S-J, Choi J-K, Lee J-S, Choi J, Kim G-T, Lee J-H (2012) Simple fabrication of transparent flexible devices using $SnO_2$ nanowires and their optoelectronic properties. Mater Lett 68:60–63
9. Zhang G, Han X, Bian W, Zhan J, Ma X (2016) Facile synthesis and high formaldehyde-sensing performance of NiO–$SnO_2$ hybrid nanospheres. RSC Adv 6(5):3919–3926
10. Gui Y-H, Wang H-Y, Tian K, Yang L-L, Guo H-S, Zhang H-Z, Fang S-M, Wang Y (2018) Enhanced gas sensing properties to $NO_2$ of $SnO_2$/rGO nanocomposites synthesized by microwave-assisted gas-liquid interfacial method. Ceram Int 44(5):4900–4907
11. Li S-M, Zhang L-X, Zhu M-Y, Ji G-J, Zhao L-X, Yin J, Bie L-J (2017) Acetone sensing of ZnO nanosheets synthesized using room-temperature precipitation. Sensors Actuators B Chem 249:611–623
12. Feng Z, Ma Y, Natarajan V, Zhao Q, Ma X, Zhan J (2018) In-situ generation of highly dispersed Au nanoparticles on porous ZnO nanoplates via ion exchange from hydrozincite for VOCs gas sensing. Sensors Actuators B Chem 255:884–890
13. Yang M, Li X, Yan B, Fan L, Yu Z, Li D (2017) Reduced graphene oxide decorated porous $SnO_2$ nanotubes with enhanced sodium storage. J Alloys Compd 710:323–330
14. Kolhe PS, Koinkar PM, Maiti N, Sonawane KM (2017) Synthesis of ag doped $SnO_2$ thin films for the evaluation of $H_2S$ gas sensing properties. Phys B Condens Matter 524:90–96
15. Gao C, Yuan S, Cao B, Yu J (2017) $SnO_2$ nanotube arrays grown via an in situ template-etching strategy for effective and stable perovskite solar cells. Chem Eng J 325:378–385
16. Chen Y, Li H, Ma Q, Che Q, Wang J, Wang G, Yang P (2018) Morphology-controlled porous α-$Fe_2O_3$/$SnO_2$ nanorods with uniform surface heterostructures and their enhanced acetone gas-sensing properties. Mater Lett 211:212–215
17. Ji X, Bai C, Zhao Q, Wang A (2017) Facile synthesis of porous $SnO_2$ quasi-nanospheres for photocatalytic degradation of rhodamine B. Mater Lett 189: 58–61
18. Wang Q, Yao N, An D, Li Y, Zou Y, Lian X, Tong X (2016) Enhanced gas sensing properties of hierarchical $SnO_2$ nanoflower assembled from nanorods via a one-pot template-free hydrothermal method. Ceram Int 42(14):15889–15896
19. Tan W, Yu Q, Ruan X, Huang X (2015) Design of $SnO_2$-based highly sensitive ethanol gas sensor based on quasi molecular-cluster imprinting mechanism. Sensors Actuators B Chem 212:47–54
20. Zhao Y, Zhang W, Yang B, Liu J, Chen X, Wang X, Yang C (2017) Gas-sensing enhancement methods for hydrothermal synthesized $SnO_2$ based sensors. Nanotechnology 28(45):452002
21. Zhou Q, Chen W, Li J, Tang C, Zhang H (2015) Nanosheet-assembled flower-like $SnO_2$ hierarchical structures with enhanced gas-sensing performance. Mater Lett 161:499–502

22. Cheng L, Ma SY, Wang TT, Luo J (2015) Synthesis and enhanced acetone sensing properties of 3D porous flower-like $SnO_2$ nanostructures. Mater Lett 143:84–87
23. Xu G, Zhang X, Cui H, Chen Z, Ding J, Zhan X (2016) Preparation of mesoporous $SnO_2$ by solvothermal method using stahlianthus involucratus leaves and application to n-butanol sensor. Powder Technol 302:283–287
24. Alinauskas L, Brooke E, Regoutz A, Katelnikovas A, Raudonis R, Yitzchaik S, Payne DJ, Garskaite E (2017) Nanostructuring of $SnO_2$ via solution-based and hard template assisted method. Thin Solid Films 626:38–45
25. Luo W, Deng J, Fu Q, Zhou D, Hu Y, Gong S, Zheng Z (2015) Nanocrystalline $SnO_2$ film prepared by the aqueous sol–gel method and its application as sensing films of the resistance and SAW $H_2S$ sensor. Sensors Actuators B Chem 217:119–128
26. Wang Q, Kou X, Liu C, Zhao L, Lin T, Liu F, Yang X, Lin J, Lu G (2017) Hydrothermal synthesis of hierarchical CoO/$SnO_2$ nanostructures for ethanol gas sensor. J Colloid Interface Sci 513:760–766
27. Li Z, Yi J (2017) Enhanced ethanol sensing of Ni-doped $SnO_2$ hollow spheres synthesized by a one-pot hydrothermal method. Sensors Actuators B Chem 243:96–103
28. Dong B, Hu W-H, Zhang X-Y, Wang J, Lu S-S, Li X, Shang X, Liu Y-R, Han G-Q, Chai Y-M, Liu C-G (2017) Facile synthesis of hollow $SnO_2$ nanospheres uniformly coated by ag for electro-oxidation of hydrazine. Mater Lett 189:9–12
29. Li Y (2018) A novel snowflake-like $SnO_2$ hierarchical architecture with superior gas sensing properties. Phys E: Low-dimen Sys and Nanostructures 96:54–56
30. Wang X, Wu Q, Jiang K, Wang C, Zhang C (2017) One-step synthesis of water-soluble and highly fluorescent $MoS_2$ quantum dots for detection of hydrogen peroxide and glucose. Sensors Actuators B Chem 252:183–190
31. Wang M, Gao Y, Dai L, Cao C, Guo X (2012) Influence of surfactants on the morphology of $SnO_2$ nanocrystals prepared via a hydrothermal method. J Solid State Chem 189:49–56
32. Talebian N, Sadeghi Haddad Zavvare H (2014) Enhanced bactericidal action of $SnO_2$ nanostructures having different morphologies under visible light: influence of surfactant. J Photochem Photobiol B 130:132–139
33. Kolhe PS, Shinde AB, Kulkarni SG, Maiti N, Koinkar PM (2018) Sonawane KM. Gas sensing performance of al doped ZnO thin film for $H_2S$ detection. J Alloys Compd 748: 6–11
34. Kuang X, Liu T, Shi D, Wang W, Yang M, Hussain S, Peng X, Pan F (2016) Hydrothermal synthesis of hierarchical $SnO_2$ nanostructures made of superfine nanorods for smart gas sensor. Appl Surf Sci 364:371–377
35. Wang J, Fan H, Yu H (2016) Synthesis of hierarchical flower-like $SnO_2$ nanostructures and their photocatalytic properties. Optik- Int J Light Electron Optics 127(2):580–584
36. Zhang M, Zhen Y, Sun F, Xu C (2016) Hydrothermally synthesized $SnO_2$-graphene composites for $H_2$ sensing at low operating temperature. Mater Sci Eng B 209:37–44
37. Wei F, Zhang H, Nguyen M, Ying M, Gao R, Jiao Z (2015) Template-free synthesis of flower-like $SnO_2$ hierarchical nanostructures with improved gas sensing performance. Sensors Actuators B Chem 215:15–23
38. Jiang XH, Ma SY, Sun AM, Xu XL, Li WQ, Wang TT, Jin WX, Luo J, Cheng L, Mao YZ (2015) 3D porous flower-like $SnO_2$ microstructure and its gas sensing properties for ethanol. Mater Lett 159:5–8
39. Xiao XY, Liu LL, Ma JH, Ren Y, Cheng XW, Zhu YH, Zhao DY, Elzatahry AA, Alghamdi A, Deng YH (2018) Ordered mesoporous tin oxide semiconductors with large pores and crystallized walls for high-performance gas sensing. Appl Mater and Interfaces 10:1871–1880
40. Cheng JP, Wang J, Li QQ, Liu HG, Li Y (2016) A review of recent developments in tin dioxide composites for gas sensing application. J Ind Eng Chem 44:1–22
41. Gao H, Zhao L, Wang L, Sun P, Lu H, Liu F, Chuai X, Lu G (2018) Ultrasensitive and low detection limit of toluene gas sensor based on $SnO_2$-decorated NiO nanostructure. Sensors Actuators B Chem 255:3505–3515